Received: 20 September 2019 | Revised: 13 April 2020 | Accepted: 15 April 2020

DOI: 10.1002/mrm.28309

FULL PAPER

Magnetic Resonance in Medicine

Fast T_2 mapping using multi-echo spin-echo MRI: A linear order approach

Yaghoub Fatemi[1] | **Habibollah Danyali**[1] | **Mohammad Sadegh Helfroush**[1] | **Houshang Amiri**[2,3]

[1]Department of Electrical and Electronics Engineering, Shiraz University of Technology, Shiraz, Iran

[2]Neuroscience Research Center, Institute of Neuropharmacology, Kerman University of Medical Sciences, Kerman, Iran

[3]Department of Radiology and Nuclear Medicine, VU University Medical Center, Amsterdam, the Netherlands

Correspondence
Houshang Amiri, Department of Radiology and Nuclear Medicine, VU University Medical Center, De Boelelaan 1117, Amsterdam, Noord-Holland 1007 MB, the Netherlands.
Emails: h.amiri@kmu.ac.ir and amiri.houshang@gmail.com

Purpose: Multi-echo spin-echo sequence is commonly used for T_2 mapping. The estimated values using conventional exponential fit, however, are hampered by stimulated and indirect echoes leading to overestimation of T_2. Here, we present fast analysis of multi-echo spin-echo (FAMESE) as a novel approach to decrease the complexity of the search space, which leads to accelerated measurement of T_2.

Methods: We developed FAMESE based on mathematical analysis of the Bloch equations in which the search space dimension decreased to only one. Then, we tested it in both phantom and human brain. Bland-Altman plot was used to assess the agreement between the estimated T_2 values from FAMESE and the ones estimated from single-echo spin-echo sequence. The reliability of FAMESE was assessed by intraclass correlation coefficients. In addition, we investigated the noise stability of the method in synthetic and experimental data.

Results: In both phantom and healthy participants, FAMESE provided accelerated and SNR-resistant T_2 maps. The FAMESE had a very good agreement with the single-echo spin echo for the whole range of T_2 values. The intraclass correlation coefficient values for FAMESE were excellent (ie, 0.9998 and 0.9860 < intraclass correlation coefficient < 0.9942 for the phantom and humans, respectively).

Conclusion: Our developed method FAMESE could be considered as a candidate for rapid T_2 mapping with a clinically feasible scan time.

KEYWORDS

extended phase graph, indirect echoes, magnetic resonance imaging, stimulated echoes, T_2 relaxation time

1 | INTRODUCTION

The T_2 relaxometry is one of the most commonly used contrast mechanisms in MRI for noninvasive diagnosis and tissue characterization. Almost every clinical MRI exam involves T_2-weighted images to detect abnormalities qualitatively.[1-3] Quantitative T_2 mapping, on the other hand, has a wide range of applications including stroke[4] and epilepsy[5]

This is an open access article under the terms of the Creative Commons Attribution-NonCommercial-NoDerivs License, which permits use and distribution in any medium, provided the original work is properly cited, the use is non-commercial and no modifications or adaptations are made.
© 2020 The Authors. *Magnetic Resonance in Medicine* published by Wiley Periodicals LLC on behalf of International Society for Magnetic Resonance in Medicine

characterization, heart[6,7] and muscle[8,9] investigation, quantification of iron content,[10] detection of cartilage physiological changes,[11-13] investigation of neurodegenerative diseases,[14-16] and differentiation of liver cancerous lesions[17] as well as prostate cancer.[18,19]

The single-echo spin-echo (SESE) technique is one of the methods for quantifying of the actual T_2 values.[20-22] One of the major disadvantages of this method is the very long scan times (on the order of tens of minutes), which makes it impractical in a clinical routine. Moreover, it is highly sensitive to the diffusion and J-coupling effects. To overcome these issues, multi-echo spin-echo (MESE) sequences are typically used for in vivo T_2 relaxometry. In MESE sequences, within one acquisition, multiple echoes are generated by applying a train of θ (typically 180°) refocusing RF pulses after a 90° RF excitation; therefore, the scan time decreases significantly (on the order of few minutes). Moreover, short-echo spacing, used in MESE sequences, results in a noticeably suppression of the diffusion[23] and J-coupling[24] effects.

In MESE sequences, to sample time points precisely along the T_2 decay curve, perfect 180° RF pulses should be applied. However, in practice, achieving a perfect refocusing pulse is challenging. Several effects such as B_1^+ inhomogeneity (finite refocusing thickness and nonrectangular slice profile), transmit calibration errors, or reduced flip angles lead to imperfect refocusing, which yields to signal contamination with stimulated and indirect echoes. This introduces the T_2 effect in T_2[21] and typically prolongs the overall signal decay, which results in substantial T_2 overestimation if a simple exponential decay model is used.[20]

To date, different postprocessing approaches have been used to cope with stimulated echo effects and to recover true T_2 values from MESE T_2 curves. These approaches generally fall into three categories. The first one improves the accuracy of the estimation by discarding some echoes from the fit[25]; however, because of the presence of stimulated and indirect echoes in later echoes, the accuracy is not high. The second category, known as model-based, simulates the stimulated and indirect echoes using the extended phase graph (EPG) algorithm[26] and integrates it into model-based reconstruction to recover true T_2 values.[21,27-31] Due to the simulation complexity, these approaches are usually computationally expensive and time-consuming; the finer the signal reconstruction, the longer the estimation time. The third approach is dictionary-based, which reproduces T_2 decay curves offline using stepwise analytical simulations for a range of T_2 values with different conditions such as B_1^+ and B_0 inhomogeneities.[20,22,32] Then, using these simulations, a database of curves will be created. Basically, the database generation is performed once, as a preprocessing step, and is used frequently as a dictionary to match pixel-by-pixel against the experimentally acquired data. A predefined dictionary can provide a faster alternative approach, but creating a comprehensive database of signals that incorporates all imaging parameters, affecting the shape of the signal, is very challenging. Moreover, generation of a comprehensive database would be a time-consuming and storage-consuming task that would also lead to noticeably increased matching time. However, it should be noted that the precision of the dictionary-based methods can be increased by measuring the B_1^+ map and removing it from the fit.[33]

In this paper, we introduce fast analysis of MESE (FAMESE) as a linear time order, $O(n)$, model-based solution for calculating T_2 relaxation time from the MESE data, which significantly decreases computation-time complexity and improves the accuracy compared with the slice-resolved extended phase graph (SEPG) model.[21] To this end, we have analyzed the MESE sequence mathematically, based on the SEPG theory using Bloch equations. After explicit extraction of the echo intensity equations, equation simplifications, and independent parameter analysis, the FAMESE model is proposed. Using FAMESE, T_2 values can be obtained by only estimating the B_1^+ parameter.

2 | METHODS

2.1 | Multi-echo spin-echo sequence formulation

The EPG model, proposed by Hennig,[26] is a powerful representation tool for depicting and understanding a variety of MR sequences. The $EPG(\cdot)$ function uses transition and relaxation rules to calculate echo amplitudes. According to this model, in an MESE sequence, the signal intensity Y_m of a voxel at the mth spin echo after a train of refocusing RF pulses with identical refocusing flip angle, α_{ref}, can be obtained by

$$Y_m = M_0 \sin(\alpha_{ex})\ EPG(T_1, T_2, \alpha_{ref}, m, esp), \quad (1)$$

where M_0, α_{ex}, T_1, T_2, and esp are the longitudinal magnetization before excitation, excitation flip angle, the spin-lattice relaxation time, the spin-spin relaxation time, and the echo spacing, respectively.

In the SEPG model, because of the variation of the RF flip angles, the signal intensity Y_m is an aggregate of echo amplitudes integrated over the slice direction z[21] as follows:

$$Y_m = \int_z M_0(z) \sin(\alpha_{ex}(z)).EPG(T_1, T_2, \alpha_{ref}(z), m, esp)\, dz, \quad (2)$$

where $\alpha_{ex}(z)$ and $\alpha_{ref}(z)$ correspond to the distribution of excitation and refocusing angles along the slice profile, which can be derived from the frequency response of the excitation

and refocusing RF pulse waveforms, obtained from the Fourier transform of their time modulations.

Due to the lack of an explicit formula for the function $EPG(.)$, it has always been calculated numerically. As depicted by Weigel[34] under the EPG framework, a MESE sequence based on the Carr-Purcell-Meiboom-Gill (CPMG) scheme can be explained by the different physical operators that modify the state matrix. In our proposed method, by applying the physical operators on the state matrix, we calculated the explicit formula for the signal intensity Y_m based on the SEPG model as follows:

$$Y_m = \sum_{i=1}^{m} M_0 \boldsymbol{S}_i\left(E_2\right) \boldsymbol{G}_{m,i}\left(E_1\right) \left[\sum_{z=1}^{Z} \sin\left(\alpha_{ex}(z)\right) \boldsymbol{\Gamma}_{m,i}\left(\alpha_{ref}(z)\right)\right] \tag{3}$$

where $\boldsymbol{S}$, $\boldsymbol{G}$, and $\boldsymbol{\Gamma}$ are vector with echo train length (ETL) elements, unit lower triangular matrix with $ETL \times ETL$ size, and lower triangular matrix with $ETL \times ETL$ size, respectively; $E_1 = \exp\left(-esp/2T_1\right)$; and $E_2 = \exp\left(-esp/2T_2\right)$. A step-by-step explanation and the proof of Equation (3) are presented in the Appendix.

To account for the RF pulse inhomogeneities, the $\alpha_{ex}(z)$ and $\alpha_{ref}(z)$ in Equation (3) are replaced by $B_1^+ \alpha_{ex}(z)$ and $B_1^+ \alpha_{ref}(z)$, where B_1^+ is a spatially varying unitless RF transmit scaling factor, which indicates the inhomogeneity of the RF transmit field as follows:

$$Y_m = \sum_{i=1}^{m} M_0 \boldsymbol{S}_i\left(E_2\right) \boldsymbol{G}_{m,i}\left(E_1\right) \left[\sum_{z=1}^{Z} \sin\left(B_1^+ \alpha_{ex}(z)\right) \boldsymbol{\Gamma}_{m,i}\left(B_1^+ \alpha_{ref}(z)\right)\right]. \tag{4}$$

Note that the B_1^+ values were constrained to $0 < B_1^+ \leq 1$ because, based on the Bloch equations of the MESE sequence, the relaxation times are identical for both $B_1^+ = 1+\delta$ and $B_1^+ = 1-\delta$. However, selective pulses are not symmetric about 180° refocusing angles.[33] In such cases, the B_1^+ can be greater than one.

2.2 | T_2 mapping procedure

2.2.1 | Theory

Assuming the ETL is equal to k and knowing that $E_2 = \exp\left(-esp/2T_2\right)$, the $M_0\boldsymbol{S}\left(E_2\right)$ term in Equation (4) will be a vector as follows (note that $\boldsymbol{S}_i\left(E_2\right)$ is the ith element of vector $\boldsymbol{S}$):

$$\begin{aligned} M_0\boldsymbol{S}\left(E_2\right) &= \begin{bmatrix} M_0E_2^2 & M_0E_2^4 & \dots & M_0E_2^{2k} \end{bmatrix}^T \\ &= \begin{bmatrix} M_0e^{-\frac{esp}{T_2}} & M_0e^{-\frac{2esp}{T_2}} & \dots & M_0e^{-\frac{kesp}{T_2}} \end{bmatrix}^T \end{aligned} \tag{5}$$

Equation (5) can be described as a discrete time domain function as follows:

$$f[n] = M_0 e^{-\frac{n\Delta\tau}{T_2}} \tag{6}$$

where $n = 1,2,\dots,k$ and $\Delta\tau$ is the sampling interval (ie, $\Delta\tau = esp$). Figure 1 plots the continuous time domain form of Equation (6), which is a T_2 decay curve with $M_0\boldsymbol{S}\left(E_2\right)$ vector as its samples at esp interval.

Therefore, we can estimate the desired T_2 relaxation time by extracting $M_0\boldsymbol{S}\left(E_2\right)$ vector elements from Equation (4) and fitting them with a mono-exponential decay curve function. To calculate the first element of the vector $\left(\text{ie}, M_0\boldsymbol{S}_1(E_2)\right)$ from Equation (4), the value of the parameter m should be set to 1, then:

$$M_0\boldsymbol{S}_1\left(E_2\right) = \frac{Y_1}{\sum_{z=1}^{Z} \sin\left(B_1^+ \alpha_{ex}(z)\right) \boldsymbol{\Gamma}_{1,1}\left(B_1^+ \alpha_{ref}(z)\right)}. \tag{7}$$

Note that the parameter B_1^+ is the only unknown value for calculating the first sample of desired T_2 decay curve. After that, the second element vector or the second sample of the T_2 decay curve can be recovered by setting $m = 2$ in Equation (4):

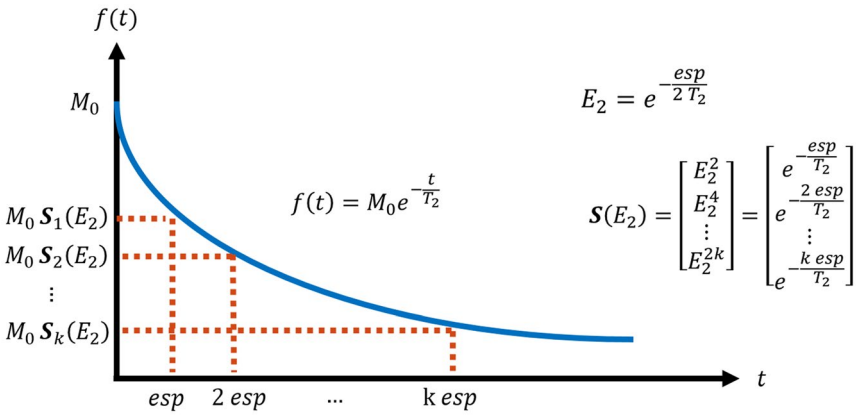

FIGURE 1 Continuous time domain form of a T_2 decay curve at different TEs. The value of M_0 indicates the longitudinal magnetization before excitation; vector S holds the T_2 decay curve samples presented in Equation (5), $E_2 = \exp\left(-t/2T_2\right)$, and $M_0S_i\left(E_2\right)$ represents the ith sample of the T_2 decay curve at ith esp

$$M_0 \boldsymbol{S}_2(E_2) = \frac{Y_2 - M_0 \boldsymbol{S}_1(E_2)\, \boldsymbol{G}_{2,1}(E_1)\, \left[\sum_z \sin\left(B_1^+ \alpha_{ex}(z)\right) \boldsymbol{\Gamma}_{2,1}\left(B_1^+ \alpha_{ref}(z)\right)\right]}{\sum_{z=1}^{Z} \sin\left(B_1^+ \alpha_{ex}(z)\right) \boldsymbol{\Gamma}_{2,2}\left(B_1^+ \alpha_{ref}(z)\right)} \tag{8}$$

Similarly, $m = k$ recovers the kth sample as follows:

$$M_0 \boldsymbol{S}_k(E_2) = \frac{Y_k - \sum_{i=1}^{k-1} M_0 \boldsymbol{S}_i(E_2)\, \boldsymbol{G}_{k,i}(E_1)\, \left[\sum_z \sin\left(B_1^+ \alpha_{ex}(z)\right) \boldsymbol{\Gamma}_{k,i}\left(B_1^+ \alpha_{ref}(z)\right)\right]}{\sum_{z=1}^{Z} \sin\left(B_1^+ \alpha_{ex}(z)\right) \boldsymbol{\Gamma}_{k,k}\left(B_1^+ \alpha_{ref}(z)\right)} \tag{9}$$

According to Equations (7-9), there are two unknown values (B_1^+ and T_1 ($E_1 = \exp(-esp/2T_1)$) to recover T_2 decay curve samples.

As reported by Lebel and Wilman[21] in a MESE decay curve, T_1 and T_2 components are indistinguishable. To compensate for this effect, they suggested that we assume $T_1 \gg T_2$. Taking this assumption into account, one can extract T_2 decay curve samples from the acquired MESE data by estimating B_1^+ value using a set of proposed equations (ie, Equations (7-9)). This means that only one parameter estimation (ie, B_1^+) is needed to estimate the true T_2 value. This indicates that the search space dimensions, using the FAMESE, can be decreased to only one dimension (ie, B_1^+). Therefore, the time complexity of the FAMESE, due to search in one dimension space, is $O(n)$, whereas, for example, the time complexity for the SEPG model is $O(n^3)$.

2.2.2 | B_1^+ estimation

To illustrate the effect of the estimated B_1^+ on recovered samples, three examples of accurate (Figure 2A), close (Figure 2B), and far (Figure 2C) estimation of B_1^+ are plotted in Figure 2. In an ideal scenario (noiseless, mono-exponential T_2, and known T_1 value), if B_1^+ is estimated correctly, the recovered samples using the proposed equations would be perfectly fitted by a mono-exponential decay curve with time constant T_2 (Figure 2A). However, when B_1^+ estimation is not precise enough, the recovered samples will deviate from the mono-exponential fit (Figure 2B,C).

To evaluate the accuracy of the B_1^+ estimation, we have proposed a method based on the singular value decomposition of the Hankel matrix. Consider a linear combination of J discrete time domain exponential function with general form of

$$g[n] = \sum_{j=1}^{J} \alpha_j e^{-\beta_j n \Delta\tau} \tag{10}$$

where J, $\Delta\tau$, α_j, and β_j are the number of exponential functions, the sampling interval, the combination weight, and the time constant, respectively. The discrete signal $g[n]$, defined by Equation (10), will be predictable to the Jth order as[35]

$$g[n] = \sum_{j=1}^{J} \gamma_j g[n-1] \tag{11}$$

This indicates that the current value of $g$and n can be predicted by J linear summation of previous values of g, $n-1$, with summation weight, γ_j. Therefore, the rank of the Hankel matrix created by $g[n]$ will equal J as follows:

$$\boldsymbol{H}[g] = \begin{bmatrix} g_1 & g_2 & \cdots & g_K \\ g_2 & g_3 & \cdots & g_{K+1} \\ \vdots & \vdots & \vdots & \vdots \\ g_{M-K+1} & g_{M-K+2} & \cdots & g_M \end{bmatrix} \tag{12}$$

where M is the length of discrete signal g and $K = M/2$. This indicates that the Hankel matrix, $\boldsymbol{H}[g]$, will have J eigenvalues if it is factorized by singular value decomposition (SVD):

$$[\boldsymbol{U}\boldsymbol{\Sigma}\boldsymbol{V}] = SVD\left(\boldsymbol{H}[g]\right), \quad \boldsymbol{H} \in \mathbb{R}^{m \times n} \tag{13}$$

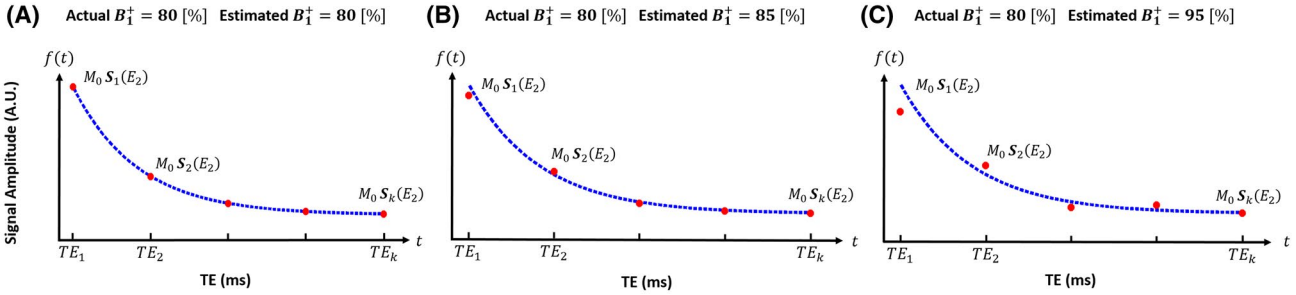

FIGURE 2 Effects of the accuracy of B_1^+ estimation on recovered samples (the graphs and samples have been theoretically simulated). A, Accurate B_1^+ estimation recovers all samples perfectly on a mono-exponential decay curve. B,C, Effects of close and far estimation from actual B_1^+ value, respectively. The dashed lines in all graphs represent a mono-exponential decay curve defined by $f(t) = M_0 \exp(-t/T_2)$

where $\boldsymbol{U}$ is an $m \times m$ real unitary matrix; $\boldsymbol{\Sigma}$ is an $m \times n$ rectangular diagonal matrix with nonnegative diagonal real numbers in decreasing order; and $\boldsymbol{V}$ is an $n \times n$ real unitary matrix. The matrix $\boldsymbol{\Sigma}$ will have J nonzero entries as long as $g[n]$ has the form of Equation (10):

$$\boldsymbol{\Sigma} = \begin{bmatrix} \sigma_1 & & & & & \\ & \ddots & & & & \\ & & \sigma_J & & & \\ & & & 0 & & \\ & & & & \ddots & \\ & & & & & 0 \end{bmatrix}, \quad \boldsymbol{\Sigma} \in \mathbb{R}^{m \times n} \quad (14)$$

where the diagonal nonzero entries σ_i are known as singular values.

The $f[n]$ in Equation (6) is a special form of $g[n]$ in Equation (10) (ie, $J=1$, $\alpha_j = M_0$, $\beta_j = 1/T_2$). Thereby, $f[n]$ is predictable to the first order. This indicates that the Hankel matrix of $f[n]$, $\boldsymbol{H}[f]$ has only one eigenvalue. Thus, if B_1^+ parameter is estimated correctly, we would expect that the rank of the Hankel matrix formed by the recovered samples to be equal to one, meaning that the $\boldsymbol{\Sigma}$ matrix derived from singular value decompensation factorization of this Hankel matrix has one nonzero entry (ie, the first diagonal entry).

If B_1^+ is not estimated correctly, the Hankel matrix will be full rank, making all diagonal entries of the $\boldsymbol{\Sigma}$ matrix nonzero. Consequently, correct estimation of B_1^+ value decreases the rank of the Hankel matrix to one. This can be used as the criterion to find true B_1^+ value. However, in practice, due to presence of the noise and unknown T_1 value, the Hankel matrix of the recovered samples will be a full rank for all B_1^+ values. This implies that all recursively recovered samples using Equations (7-9) for all B_1^+ values will not be fitted by a pure mono-exponential function; therefore, all diagonal entries of the $\boldsymbol{\Sigma}$ matrix will be nonzero. However, as shown in Figure 2, if the estimated B_1^+ value is closer to the true value, the proximity of the recovered samples to pure mono-exponential decay curve will be increased, and then all eigenvalues of the $\boldsymbol{\Sigma}$ matrix, except the first one, tends to zero. Therefore, minimizing all such eigenvalues is defined as the criterion to estimate the optimum B_1^+ value. The entire flowchart of the FAMESE method is illustrated in Figure 3.

It should be noted that the proposed B_1^+ estimation procedure is presented in such a way that errors, due to constant T_1 assumption and noise effects, are more likely to be imposed on the optimum B_1^+ than on T_2. In fact, the optimum B_1^+ that minimizes the objective eigenvalues will be

$$optimal\ B_1^+ = actual\ B_1^+ + T_1\ assumption error + noise\ effect \quad (15)$$

Therefore, the estimated B_1^+ map should not be mistaken with the actual B_1^+ map.

2.3 | Magnetic resonance imaging experiments

We tested our developed FAMESE method in vitro and in vivo using MR images acquired on a 1.5T MR scanner (Magnetom Avanto; Siemens Healthcare, Erlangen, Germany). To assess the accuracy of FAMESE in the phantom and in humans,

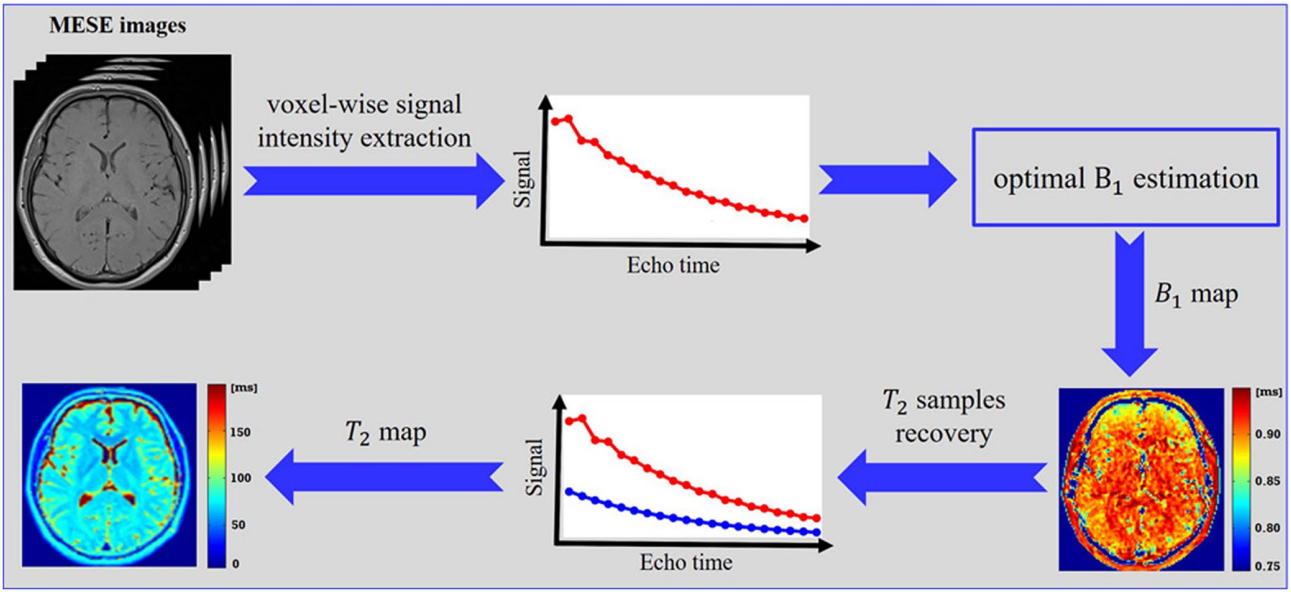

FIGURE 3 Scheme showing T_2 mapping using the proposed method (fast analysis of multi-echo spin echo [FAMESE]). Note that the "blue" graph is the FAMESE output, which corrects the T_2 decay curve used for the conventional exponential fit (red). Abbreviation: MESE, multi-echo spin echo

both MESE and SESE were acquired during the same scanning session. In the SEPG model and proposed FAMESE, the distributions of the excitation, $\alpha_{ex}(z)$, and refocusing, $\alpha_{ref}(z)$, angles along the slice profile are needed as input. One can obtain these directly from the frequency response of the RF pulses data from the scanner. Because access to these data are restricted on most clinical scanners, we used the StimFit toolbox[36] (with default settings), which uses Fourier transform to simulate the slice-selective excitation and refocusing pulses. These flip angle distributions are used in both SEPG and FAMESE, for all experiments. It should be mentioned that using SEPG with Shinnar–Le Roux[37] approximation of slice profiles, as compared with the Fourier transform approach, will improve the accuracy of T_2 estimation.[33] In such a case, the results of FAMESE will also improve.

2.3.1 | In vitro MR experiments

A four-channel head coil was used to perform in vitro phantom scans. Nine tubes of different $MnCl_2$ concentrations (tube #1, 0.070; tube #2, 0.135; tube #3, 0.270; tube #4, 0.405; tube #5, 0.540; tube #6, 0.675; tube #7, 0.800; tube #8, 1.000; tube #9, 0.540 mM), mimicking a range of T_2 values in human tissues (liver, heart, brain, and prostate[20,25]), were prepared and placed in an 18 × 18 cm^2 MR-compatible holder. The diameter of each test tube was 4 cm and the distance between them was about 3 cm. To assess variation of the B_1^+ field inhomogeneity, tubes #5 and #9 were prepared with identical $MnCl_2$ concentrations that were positioned at two different locations (distance ≈ 11 cm). Axial 2D MESE and SESE images of the phantoms were acquired with identical imaging sequence parameters as follows: TR = 1500 ms, TE = 12, 24, …, 60 ms, ETL = 5, matrix size = 128 × 128, FOV = 200 × 200 mm^2, slice thickness = 3 mm, refocusing pulse $\alpha_{ref} = 180°$, acquisition bandwidth BW_{acq} = 200 Hz/Px, and number of slices = 1. To investigate the SNR stability, the scans were repeated two more times: the first time (referred to as experiment No. 2) with the same sequence parameters as previously and changing only the slice thickness to 6 mm, and the second time (referred to as experiment No. 3) with the same sequence parameters as previously and changing only the matrix size to 192 × 192.

2.3.2 | In vivo MR experiments

Four healthy volunteers participated in the study after completing the informed consent form. The study was conducted with the approval of the Institutional Review Board. Axial single-slice 2D MESE and SESE images were acquired using the identical imaging sequence parameters as follows: TR = 1500 ms, TE = 12, 24, …, 60 ms, matrix size = 128 × 128, FOV = 220 × 220 mm^2, slice thickness = 3 mm, BW_{acq} = 200 Hz/Px, $\alpha_{ref} = 180°$, and number of slices = 1.

2.3.3 | Statistical analysis

Bland-Altman plot[38] was used to measure the agreement between the estimated T_2 values with the SESE acquisition scheme. For this purpose, nine regions of interest (ROIs, in total 27 ROIs in three repeated phantom experiments), each about 4.7 × 4.7 mm^2, were selected in the center of each tube on the phantom MR images. For a more comprehensive assessment of FAMESE in humans, in each individual's brain images, 24 ROIs (96 total ROIs in 4 subjects) were randomly selected. An example of the distribution of the randomly selected ROIs in the brain is presented in Figure 4F (the ROIs for all subjects are presented as Supporting Information Figure S1). It should be noted that because all ROIs in human subjects were selected randomly and distributed over the whole brain uniformly, some of the ROIs could be located in the positions including more than one tissue type (eg, the white and gray matter). To minimize this effect, the size of the ROIs were chosen as small as about 4.7 × 4.7 mm^2. Moreover, to determine the reliability of the T_2 values estimated by the FAMESE, SEPG model, and conventional exponential fit, the intraclass correlation coefficients (ICCs) for absolute agreement were calculated.[39] The ICC and Bland-Altman plots were generated using *MATLAB* (The MathWorks, Natick, MA).

2.4 | Performance analysis

To assess the accuracy and precision of the FAMESE in the presence of noise, the T_2 stability was assessed at different noise levels. To this end, a set of MESE T_2 curves was simulated using the Bloch equations at different levels of zero-mean Gaussian white noise with the following parameters: TE = 12, 24, 36, 48, 60 ms; T_1 = 3000 ms; T_2 = 60, 80, and 100 ms; B_1^+ = 80%, 90%, and 100%; and SNR = 25, 30, 40, 60, and 100. To estimate the accuracy (mean value) and precision (SD) for each set of T_2, B_1^+, and SNR, 500 MESE curves were simulated. In addition, to directly show the effect of different refocusing flip angles on T_2 measurement, 500 MESE curves were simulated for T_2 = 80, 100, and 120 ms using the following parameters: SNR = 35; TE = 12, 24, 36, 48, and 60 ms; and T_1 = 3000 ms. The refocusing flip angles ranged from 110° to 220° (step size = 10°).

3 | RESULTS

3.1 | Magnetic resonance imaging T_2 mapping

The T_2 relaxometry results of the phantom experiments are presented in Table 1. In all results, for completeness, we have included the results of the conventional exponential

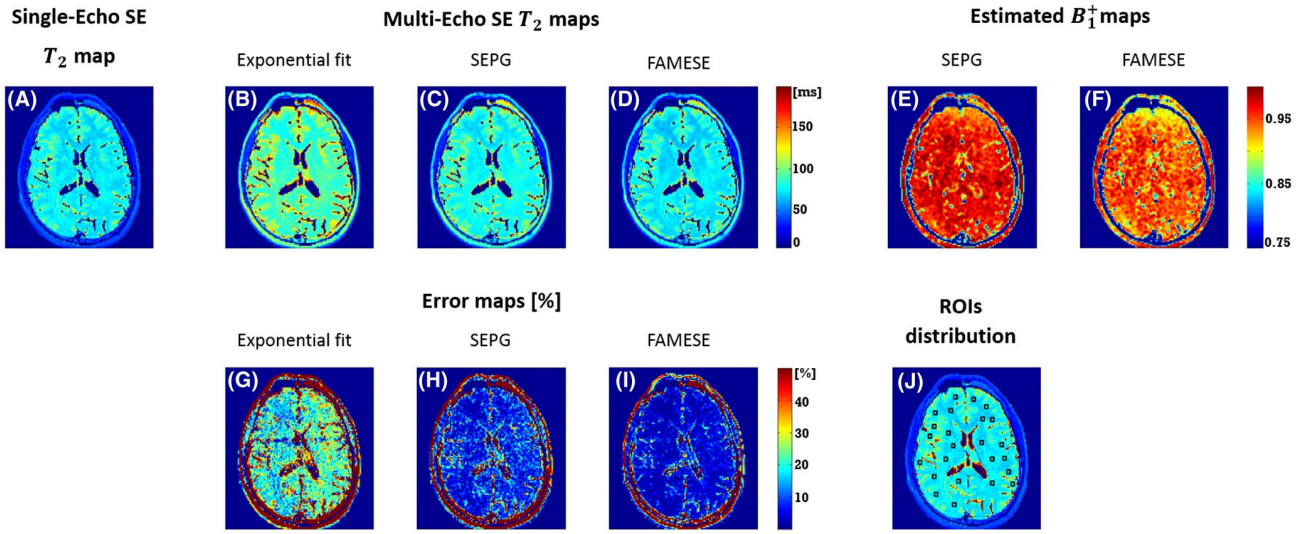

FIGURE 4 Representative brain T_2 maps of a healthy volunteer obtained from a conventional exponential fitting on single-echo spin echo (SESE) (A), MESE data (B), and slice-resolved extended phase graph (SEPG) model (C) as well as the proposed method FAMESE (D). Estimated B_1^+ maps for FAMESE and SEPG are presented in (E) and (F), respectively. The error maps for different methods are shown in (G)-(I). J, Example of the distribution of the randomly selected regions of interest (ROIs) for Bland-Altman and intraclass correlation coefficient (ICC) analyses

fit. Although we were not aiming to compare our method with the exponential fit, it is worth mentioning that the results of the conventional exponential fit could improve if one skips the first echo.[40,41]

Any deviation from perfect 180° RF refocusing pulse in MESE sequences leads to signal contamination with stimulated and indirect echoes, and yields to T_2 overestimation when a conventional exponential decay is used. In fact, the B_1^+ inhomogeneity and its effect on echoes give rise to a bias in the approximation of the T_2 relaxation time. Such a bias (about 18% on average) can be seen by comparing the T_2 relaxation times obtained by the conventional exponential fitting with the SESE sequence (see Table 1). This error for the SEPG is about 4%. The FAMESE, on the other hand, significantly decreases the bias effect (to less than 1%) and therefore improves the accuracy owing to the mathematical analysis of the B_1^+ inhomogeneity on the MESE pulse sequence.

As presented in Table 1, The SEPG model provides better accuracy against the conventional exponential fit. Owing to the decreasing search-space dimensions and therefore preventing the propagation errors, the FAMESE provides more accurate and more resistant T_2 values compared with the other two methods. Moreover, estimated T_2 values of tubes #5 and #9 are similar, as was expected for identical concentrations.

A representative example of the in vivo T_2 mapping is presented in Figure 4. It compares the maps derived from exponential fitting on the SESE images (Figure 4A) to that from applying conventional exponential fitting, SEPG model, and FAMESE on the MESE images (Figure 4B-D). Similar to the phantom results, FAMESE provided much better estimation of T_2 relaxation times compared with the conventional exponential fitting and the SEPG model. To better depict the differences, difference maps (Figure 4G-I) were calculated by dividing the absolute difference between SESE and MESE maps by the reference SESE map. In addition, the generated B_1^+ maps for both FAMESE and SEPG are shown in Figure 4E,J. It is worth mentioning that the B_1^+ map is defined here by Equation (15) and should not be mistaken by the actual B_1^+ map.

To better demonstrate the FAMESE performance in different brain regions, the average T_2 values in 10 different selected ROIs with 3 × 3 neighboring voxels (as presented in Supporting Information Figure S2) were calculated in one of the human subjects (Table 2). The results revealed excellent agreement between FAMESE and the ones extracted from SESE sequence (0.87% ± 0.61% error, on average), whereas the T_2 values obtained by conventional exponential fit and SEPG model, using MESE data, were 14.48% ± 2.19% and 2.22% ± 0.86% (on average) overestimated, respectively. Similar to the phantom study, the SEPG model provided better T_2 values compared with the conventional exponential fit. In these experiments, as in the phantom experiments, the FAMESE not only estimates T_2 values with highest accuracy, but it also preserves its stability.

In Figure 5, the Bland-Altman plots are presented for all ROIs (ie, 27 ROIs in phantom [9 in each experiment]) and 96 ROIs in humans [27 in each subject]). The limits of agreement for the exponential fit were quite high (for phantoms [–17, 36] and for human subjects [–4, 41]) specifically for T_2 values greater than 100 ms. The limits of agreement decreased using the SEPG model (for phantoms [–2, 4] and for human subjects [–1, 6]). The FAMESE, however, had a very good agreement with the SESE for the whole range of

TABLE 1 Phantom $T_2 \pm$ SD values for three sets of experiments

Tube No.	Experiment No.	SESE (ms)	MESE		
			Exp. fit (ms)	SEPG (ms)	FAMESE (ms)
1	1	148.96 ± 1.09	181.25 ± 1.03	145.51 ± 0.26	147.78 ± 0.26
	2	145.85 ± 0.39	183.47 ± 0.54	148.81 ± 0.72	149.59 ± 0.56
	3	146.64 ± 1.13	180.40 ± 3.22	148.71 ± 2.12	148.22 ± 2.02
2	1	85.12 ± 0.68	100.48 ± 0.22	87.17 ± 0.25	85.97 ± 0.13
	2	85.93 ± 0.55	101.74 ± 0.04	87.19 ± 0.19	86.56 ± 0.13
	3	84.83 ± 0.38	101.15 ± 0.87	87.67 ± 0.99	86.34 ± 0.81
3	1	45.41 ± 0.06	52.04 ± 0.13	45.59 ± 0.20	45.28 ± 0.12
	2	45.67 ± 0.07	52.64 ± 0.09	46.06 ± 0.17	45.73 ± 0.11
	3	45.93 ± 0.08	53.00 ± 0.18	46.33 ± 0.28	46.10 ± 0.09
4	1	29.64 ± 0.10	34.02 ± 0.07	29.86 ± 0.06	29.76 ± 0.05
	2	30.22 ± 0.08	34.66 ± 0.04	30.26 ± 0.05	30.24 ± 0.02
	3	30.26 ± 0.17	34.79 ± 0.28	30.57 ± 0.21	30.40 ± 0.18
5	1	22.73 ± 0.11	26.20 ± 0.05	22.85 ± 0.06	22.83 ± 0.05
	2	22.95 ± 0.07	26.63 ± 0.02	23.17 ± 0.03	23.15 ± 0.02
	3	23.24 ± 0.15	26.94 ± 0.15	23.64 ± 0.35	23.48 ± 0.16
6	1	18.12 ± 0.15	21.19 ± 0.05	18.60 ± 0.05	18.33 ± 0.03
	2	18.46 ± 0.03	21.53 ± 0.02	18.72 ± 0.04	18.56 ± 0.01
	3	18.33 ± 0.13	21.52 ± 0.09	18.83 ± 0.19	18.64 ± 0.09
7	1	15.52 ± 0.11	18.37 ± 0.03	15.83 ± 0.09	15.68 ± 0.03
	2	15.70 ± 0.02	18.58 ± 0.02	15.86 ± 0.03	15.79 ± 0.01
	3	15.77 ± 0.26	18.69 ± 0.01	16.00 ± 0.07	15.92 ± 0.03
8	1	12.16 ± 0.12	14.35 ± 0.07	15.15 ± 0.12	11.82 ± 0.10
	2	12.01 ± 0.07	14.63 ± 0.01	15.04 ± 0.03	12.02 ± 0.02
	3	12.39 ± 0.11	14.52 ± 0.11	15.09 ± 0.11	12.00 ± 0.07
9	1	22.54 ± 0.14	25.86 ± 0.02	22.72 ± 0.04	22.55 ± 0.02
	2	22.67 ± 0.04	26.06 ± 0.02	22.80 ± 0.03	22.67 ± 0.02
	3	22.87 ± 0.12	26.34 ± 0.05	23.16 ± 0.09	22.99 ± 0.05
Average error (%)			**16.94 ± 2.35**	**4.04 ± 7.74**	**0.90 ± 0.81**
			17.98 ± 3.69	**3.74 ± 8.06**	**0.61 ± 0.80**
			17.41 ± 2.58	**3.95 ± 6.72**	**1.23 ± 0.88**

Note: The values were estimated either by exponential fit on the SESE data as reference values or by applying conventional exponential fit, SEPG model, and FAMESE on the ROIs defined at the center of each tube in MESE data. In the last row, for each estimated MESE T_2 value, averages of relative errors were computed by dividing the absolute difference between estimated and reference T_2 values by the corresponding reference values (indicated by the boldfaced values).

T_2 values revealed, with very narrow limits of agreement (for phantom [–1, 2] and for human brain subjects [–0.5, 3]).

The ICC values for absolute agreement between the T_2 values obtained from the SESE technique and the ones calculated using FAMESE are presented in Figure 6. The ICC values using the conventional exponential fit and the SEPG model were 0.9631 and 0.9993 for the phantoms, and $0.4425 < \text{ICC} < 0.5617$ and $0.9672 < \text{ICC} < 0.9803$ for the humans, respectively. The FAMESE improved these ICC values to 0.9998 and $0.9860 < \text{ICC} < 0.9942$ for the phantom and humans, respectively. The ICC values of the FAMESE also proved its good agreement and good stability in both phantom and human brain images.

3.2 | Accuracy and precision analysis

The accuracy and precision analysis of the developed FAMESE method, in the presence of noise, are presented in Figure 7. The FAMESE significantly improved the accuracy for 80%, 90%, and 100% B_1^+ inhomogeneities, with the average errors of 0.50%, 0.40%, and 0.14%, respectively,

TABLE 2 Quantitative analysis of T_2 values in 10 selected ROIs in a healthy volunteer (see Supporting Information Figure S2)

	T_2 value (ms)			
		MESE		
ROI No.	SESE	Exp. fit	SEPG	FAMESE
1	92.29 ± 3.20	109.3 ± 2.60	94.12 ± 2.47	92.56 ± 1.15
2	77.00 ± 1.39	91.52 ± 1.43	78.18 ± 1.86	77.32 ± 0.55
3	66.88 ± 1.66	80.25 ± 2.91	68.71 ± 2.61	66.94 ± 0.42
4	85.60 ± 2.62	104.6 ± 2.89	88.25 ± 1.83	87.37 ± 1.2
5	74.23 ± 2.42	89.72 ± 0.68	77.94 ± 1.07	75.79 ± 0.89
6	75.34 ± 1.31	90.05 ± 2.07	78.91 ± 1.24	76.89 ± 0.89
7	71.73 ± 0.73	83.92 ± 2.02	73.81 ± 1.98	72.82 ± 0.51
8	75.04 ± 1.71	88.42 ± 4.02	77.07 ± 4.51	75.94 ± 0.84
9	82.92 ± 0.23	95.60 ± 1.68	84.15 ± 1.74	83.52 ± 0.61
10	76.54 ± 1.21	88.96 ± 1.60	78.66 ± 1.46	77.08 ± 0.85
Average error (%)		**14.48 ± 2.19**	**2.22 ± 0.86**	**0.87 ± 0.61**

Note: The boldfaced values indicate the averages and the SD of relative errors.

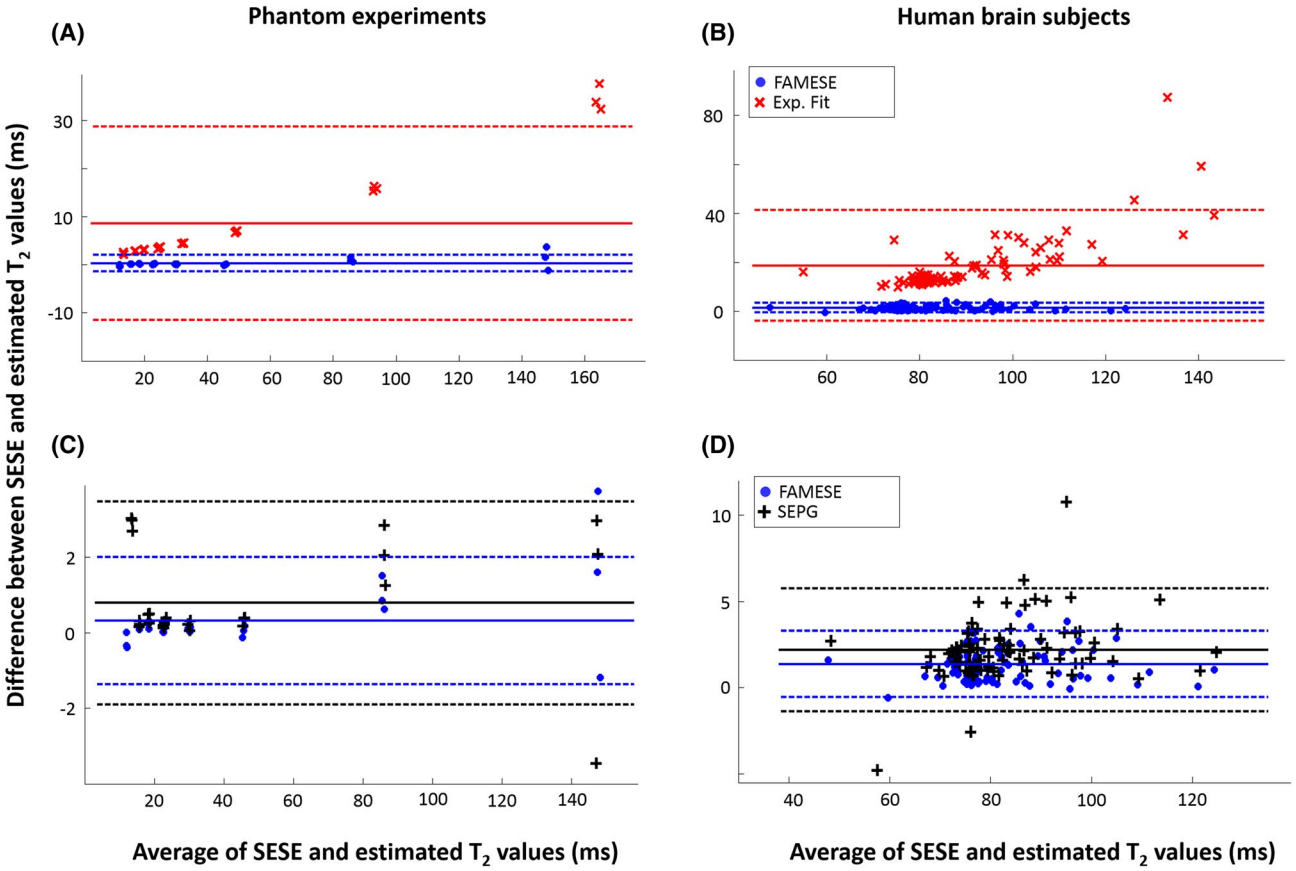

FIGURE 5 The Bland-Altman plots for 27 ROIs in phantom (nine in each experiment) (A,C) and 96 ROIs in the brain of all healthy volunteers (27 in each subject) (B,D) to illustrate the agreement between SESE with FAMESE (blue), SEPG (black), and the exponential fit (red) obtained from the MESE data. Dotted lines represent the limits of agreement

as compared with the conventional exponential fit (average errors = 31.11%, 15.53%, and 9.79%) and the SEPG model (average errors = 2.57%, 2.12%, and 1.87%), for all predefined ranges of T_2 values and the SNRs between 25 and 100. A similar trend was seen in the precision with better SDs, with the average errors of 1.29%, 0.96%, and 0.38% for

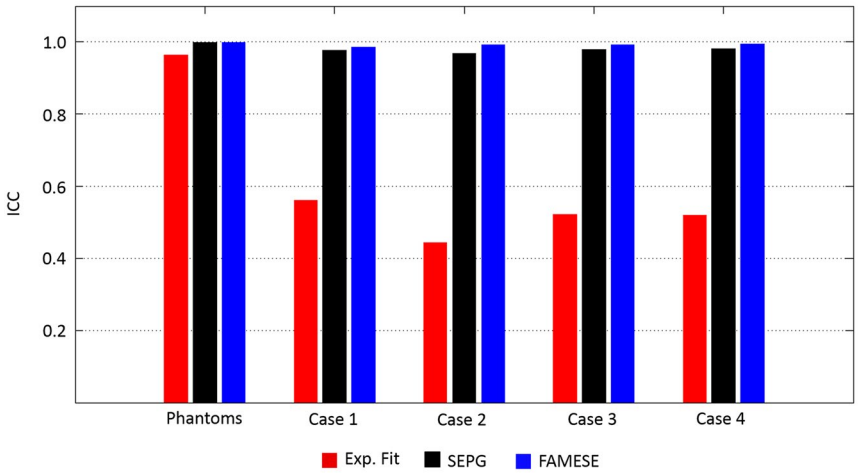

FIGURE 6 Intraclass correlation coefficients between SESE and estimated T_2 relaxation times by conventional exponential fit (red), SEPG model (black), and the proposed FAMESE (blue) for the phantom (averaged over all nine ROIs for the three experiments) and 24 randomly selected ROIs of human brain in 4 healthy volunteers

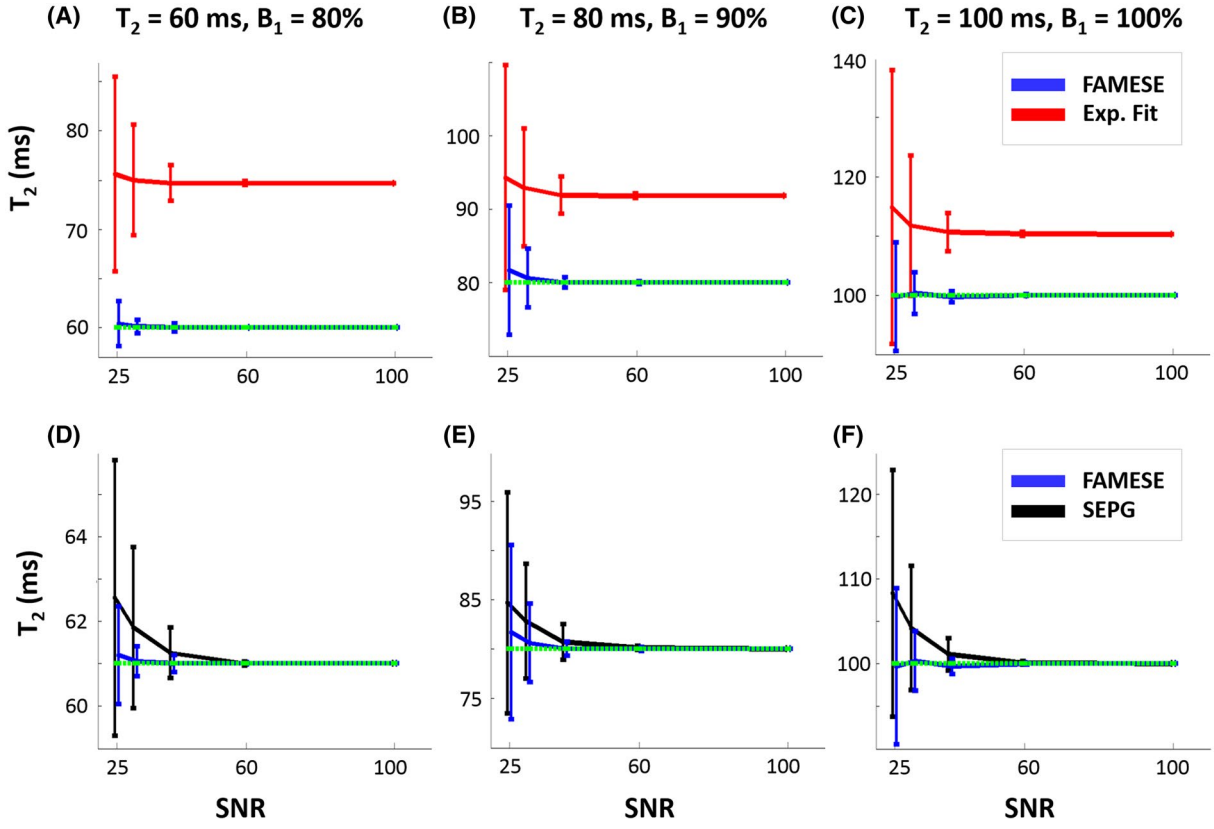

FIGURE 7 Graphical illustration of the accuracy (mean value) and precision (SD) to make a comparison of the proposed method FAMESE (blue) against the SEPG model (black) as a function of the SNR. The underlying T_2 values are shown with green dashed lines

the FAMESE model, 3.21%, 2.67%, and 2.26% for the SEPG model, and 5.86%, 2.73%, and 1.92% for the conventional exponential fit.

The effect of the refocusing flip angle on the estimation of the T_2, by both FAMESE and SEPG, is presented in Figure 8. It is evident that FAMESE provides more reliable and stable results, specifically for the refocusing pulses greater than 180°.

4 | DISCUSSION

The T_2 relaxation time serves as an important biomarker for noninvasive tissue characterization. However, its rapid and accurate quantification in a clinical setting remains challenging. The SESE sequence measures T_2 values accurately at the cost of long scanning time. The MESE sequences, on the other hand, decrease scanning time noticeably with the loss

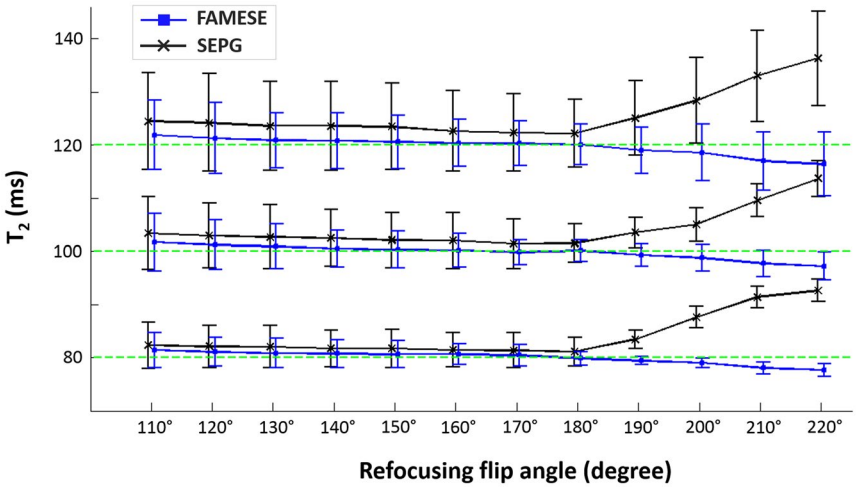

FIGURE 8 Effect of different flip angles on the estimated T_2 values by FAMESE (blue) and SEPG (black) methods. The underlying T_2 values are shown with green dashed lines

of accuracy. Here, we introduced FAMESE as a novel post-processing approach to extract quick and reliable T_2 relaxation times obtained from MESE data with estimation of only one parameter.

The model-based methods have also been introduced for improving T_2.[21,29,30] They simulate T_2 decay curves by means of simulation tools such as EPG, using a set of variables (ie, T_2, B_1^+, and M_0). Such methods need simultaneous search through the variables' ranges. Due to the simulation complexity, the estimation of parameters simultaneously is a time-consuming task (for T_2, B_1^+, and M_0, the time complexity will be $O(n^3)$). In fact, the model and dictionary-based methods endeavor to find the optimal solution in a high-dimensional search space, whereas FAMESE decreases the dimension to one (ie, B_1^+) which accelerates the searching process (the time complexity of the FAMESE is $O(n)$). As a numerical example, if $20 \le T_2 \le 140\ s.t.\ \delta T_2 = 0.01$, $0.2 \le B_1^+ \le 1.0\ s.t.\ \delta B_1^+ = 0.01$, and $200 \le M_0 \le 3000\ s.t.\ \delta M_0 = 1$, then the search space for the SEPG model will be $12{,}000 \times 80 \times 2{,}800 = 2{,}688{,}000{,}000$, whereas using FAMESE the search space will be decreased to 80. The computation time using FAMESE, to generate the T_2 map, was about 1 minute on a desktop PC with Intel Core i3-330M CPU and 3 GB memory running *MATLAB* R2013a.

More importantly, the estimation error of one parameter propagates to the other parameters, known as propagation effect. In contrast, by reducing the search-space dimensions to one dimension, FAMESE accelerates the estimation process and prevents the propagation error effects, giving rise to a more reliable T_2 relaxation time. Moreover, the fact that FAMESE is fast, accurate, and independent of echo spacing, makes it of great interest in the clinical settings.

In the T_2 mapping process using FAMESE, two extra parameters (ie, B_1^+ and M_0 [as an estimation of the proton density]) are also generated. These parameters can complement the T_2 map information. It should be noted that in the estimations of these two parameters, only RF pulse inhomogeneities are considered, whereas other second-order distorting factors such as B_0 inhomogeneities, T_1 relaxation, and diffusion could also have an impact on the T_2 calculation. However, interestingly, the good agreement of the estimated T_2 map between FAMESE and SESE revealed the negligible effect of the second-order distortions on the T_2 relaxation time when using FAMESE. Nevertheless, incorporating them into the estimation process could potentially improve the accuracy. For example, embedding a B_1^+ filed map (such as in Kumar et al[42]) into the FAMESE could lead to better estimation of B_1^+ and therefore more precise calculation of the T_2 relaxation time.

To investigate the effect of B_1^+ variation, tubes #5 and #9 of the phantom with identical concentrations were placed in two different locations in the coil. The corresponding T_2 values were slightly different, which could be related to the factors affecting the T_2, such as the noise. Finding similar T_2 values for both tubes confirms the minimization of the B_1^+ effect using both SEPG and FAMESE. It should be noted that at 1.5 T the B_1^+ variation for relatively closely spaced tubes could be small; therefore, to evaluate the effect of the variation, this needs to be tested at higher magnetic field strength, such as at 3 T.

It has been shown that the bias of the conventional exponential fit increases for higher T_2 values.[20] We observed the same effect (Figure 5). By comparing the Bland-Altman plots of conventional exponential fit, SEPG model, and FAMESE model, it can be seen that FAMESE not only has a very good agreement with the SESE, but it also significantly removed the biases for higher T_2 values and provided a good stability for the whole range of T_2 values.

The ICC is a value that measures the reliability reflecting the degree of correlation and the agreement between measurements. It ranges between 0 and 1, with the ICC = 1 being the best agreement. The FAMESE provides better ICC values than the conventional exponential fitting and the SEPG model. Because the ROIs are distributed randomly in all brain locations for all human subjects and there is

nonuniform B_1^+ distribution (Figure 4E), the ICC values of the conventional exponential fitting method vary in different cases ($\Delta ICC = 0.52$). The SEPG and FAMESE methods narrow down these variations significantly ($\Delta ICC = 0.03$ and $\Delta ICC = 0.01$, respectively). The ICC values of the proposed method show that FAMESE, in addition to the good reliability, provides more stable T_2 values in comparison to the conventional exponential fitting and the SEPG model.

The SNR stability is a key factor to make an approach deployable in a real imaging routine because of its dependency on several parameters such as FOV, slice thickness, bandwidth, and magnetic field strength. Such parameters and therefore the SNR instability could lead to incorrect T_2 estimation and misinterpretation as a result. Thus, it is important for the developed methods to be noise resistant. As shown in Figure 7A-C, the conventional exponential method not only extracts the T_2 values with a bias, but it also is very sensitive to the noise. The proposed FAMESE, however, eliminates the bias while preserving its resistance to the noise. As demonstrated in Figure 7D-F, decreasing the propagation effects by FAMESE leads to better accuracy and decreases the SD values compared with the SEPG model. As shown in Figure 8, for the ranges of the flip angles tested, FAMESE demonstrated to be less sensitive to the refocusing flip angle as compared with SEPG, specifically for the flip angles greater than 180°. This is of importance in clinical practice, especially at higher field strengths such as 3 T and 7 T.

To further investigate SNR and noise stability experimentally, we scanned the phantom with three different settings within the same scanning session. As indicated in Table 1, both SEPG and FAMESE provided stable T_2 values. However, the results of the FAMESE demonstrate lower SD in addition to improving the accuracy. The higher SD in SEPG is likely due to the short ETL used in our experiments, whereas the FAMESE proved to be less sensitive to this.

It is important to note that in addition to the RF transmit field inhomogeneity and the stimulated and indirect echoes, there are other factors that cause bias in T_2 relaxation times, such as magnetization transfer,[43,44] diffusion[23] and J-coupling[24] effects, which may modify our model. However, we assume such effects to be present in all methods used. For instance, possible diffusion weighting of the image caused by imaging gradients may result in underestimation of T_2 when using a multi-echo sequence, but this effect has been shown to be present regardless of the technique used to analyze the data.[45]

In this research, we had some limitations. We assumed that $T_1 \gg T_2$, but this may not be the case for all phantom tubes in which the T_1 relaxation times vary with $MnCl_2$ concentration. Also, we set ETL = 5 with maximum TE = 60 ms, which could potentially add bias when estimating long T_2 components. However, identical parameters were used for all methods, and FAMESE performed well even for estimating long T_2 components (eg, tubes #1 and #2). In addition, to have a feasible scan time (specifically for SESE images), TR = 1500 ms was used, which could have an impact on T_2 measurement, such as due to partial recovery. Finally, we have tested our method on a single slice; therefore, it would be of clinical interest to investigate its performance on multislice imaging, knowing that then the scan time would be a challenge.

5 | CONCLUSIONS

The FAMESE model, by decreasing the search space dimensions and therefore precluding from error propagation effect, not only accelerates the estimation process, but it also provides robust and SNR-resistant T_2 maps. This makes FAMESE a potential method for reliable measurement of T_2 relaxation times in various pathological conditions in the clinical routine, where quantitative MRI plays an important role. To this end, it would be interesting to test FAMESE in different diseases. Furthermore, generalizations such as multiple T_2 components[29,42] can be applied to FAMESE. Here, we assumed that T_2 decays are mono-exponential, although it can be considered as a multi-exponential function to be decomposed for extracting multiple T_2 components. Of interest, FAMESE can be applied easily to other experimental parameters such as T_1, to robustly and rapidly estimate them.

ACKNOWLEDGMENTS

The authors thank Zahra Sharifi for significant assistance with data collection and Zahra Farshidfar for valuable discussions at the early stage of the research.

ORCID

Houshang Amiri https://orcid.org/0000-0003-4086-5255

REFERENCES

1. Knight MJ, Wearn A, Coulthard E, Kauppinen RA. T2 relaxometry and diffusion tensor indices of the hippocampus and entorhinal cortex improve sensitivity and specificity of MRI to detect amnestic mild cognitive impairment and Alzheimer's disease dementia. *J Magn Reson Imaging*. 2019;49:445-455.
2. Papadaki E, Kavroulakis E, Kalaitzakis G, et al. Age-related deep white matter changes in myelin and water content: A T2 relaxometry study. *J Magn Reson Imaging*. 2019;50:1393-1404.
3. Gallo MC, Pedoia V, Link TM, Souza RB, Majumdar S. 3-year longitudinal assessment of hip cartilage using T1ρ and T2 relaxometry. *Osteoarthritis Cartilage*. 2016;24:S266-S267.
4. McGarry BL, Rogers HJ, Knight MJ, et al. Stroke onset time estimation from multispectral quantitative magnetic resonance imaging in a rat model of focal permanent cerebral ischemia. *Int J Stroke*. 2016;11:677-682.
5. Winston GP, Vos SB, Burdett JL, Cardoso MJ, Ourselin S, Duncan JS. Automated T2 relaxometry of the hippocampus for temporal lobe epilepsy. *Epilepsia*. 2017;58:1645-1652.

6. Aliotta E, Moulin K, Zhang Z, Ennis DB. Simultaneous measurement of T2 and apparent diffusion coefficient (T2+ADC) in the heart with motion-compensated spin echo diffusion-weighted imaging. *Magn Reson Med*. 2018;79:654-662.
7. Baessler B, Luecke C, Klingel K, et al. P2583Texture analysis and machine learning applied on cardiac magnetic resonance T2 mapping: incremental diagnostic value in biopsy-proven acute myocarditis. *Eur Heart J*. 2017;38:544.
8. Wokke BH, Bergen JCVD, Hooijmans MT, Verschuuren JJ, Niks EH, Kan HE. T2 relaxation times are increased in Skeletal muscle of DMD but not BMD patients. *Muscle Nerve*. 2016;53:38-43.
9. Marty B, Toussaint M, Gilles R, Wahbi K, Carlier P. Skeletal muscle tissue characterization of a large cohort of patients with Becker muscular dystrophy using quantitative NMR imaging. *Neuromuscul Disord*. 2017;27:S126.
10. Ghassaban K, Liu S, Jiang C, Haacke EM. Quantifying iron content in magnetic resonance imaging. *Neuroimage*. 2019;187:77-92.
11. Wang X, Wrigley TV, Bennell KL, et al. Cartilage quantitative T2 relaxation time 2–4 years following isolated anterior cruciate ligament reconstruction. *J Orthop Res*. 2018;36:2022-2029.
12. Soellner ST, Goldmann A, Muelheims D, Welsch GH, Pachowsky ML. Intraoperative validation of quantitative T2 mapping in patients with articular cartilage lesions of the knee. *Osteoarthritis Cartilage*. 2017;25:1841-1849.
13. Monu UD, Jordan CD, Samuelson BL, Hargreaves BA, Gold GE, McWalter EJ. Cluster analysis of quantitative MRI T2 and T1ρ relaxation times of cartilage identifies differences between healthy and ACL-injured individuals at 3T. *Osteoarthritis Cartilage*. 2017;25:513-520.
14. Diaz-de-Grenu LZ, Acosta-Cabronero J, Pereira JMS, Pengas G, Williams GB, Nestor PJ. MRI detection of tissue pathology beyond atrophy in Alzheimer's disease: Introducing T2-VBM. *NeuroImage*. 2011;56:1946-1953.
15. Focke NK, Yogarajah M, Symms MR, Gruber O, Paulus W, Duncan JS. Automated MR image classification in temporal lobe epilepsy. *NeuroImage*. 2012;59:356-362.
16. Shepherd TM, Kirov II, Charlson E, et al. New rapid, accurate T2 quantification detects pathology in normal-appearing brain regions of relapsing-remitting MS patients. *NeuroImage Clin*. 2017;14:363-370.
17. Cieszanowski A, Anysz-Grodzicka A, Szeszkowski W, et al. Characterization of focal liver lesions using quantitative techniques: Comparison of apparent diffusion coefficient values and T2 relaxation times. *Eur Radiol*. 2012;22:2514-2524.
18. Dregely I, Margolis DAJ, Sung K, et al. Rapid quantitative T2 mapping of the prostate using three-dimensional dual echo steady state MRI at 3T. *Magn Reson Med*. 2016;76:1720-1729.
19. Yamauchi FI, Penzkofer T, Fedorov A, et al. Prostate cancer discrimination in the peripheral zone with a reduced field-of-view T2-mapping MRI sequence. *Magn Reson Imaging*. 2015;33:525-530.
20. Ben-Eliezer N, Sodickson DK, Block KT. Rapid and accurate T2 mapping from multi–spin-echo data using Bloch-simulation-based reconstruction. *Magn Reson Med*. 2015;73:809-817.
21. Lebel RM, Wilman AH. Transverse relaxometry with stimulated echo compensation. *Magn Reson Med*. 2010;64:1005-1014.
22. Neumann D, Blaimer M, Jakob PM, Breuer FA. Simple recipe for accurate T(2) quantification with multi spin-echo acquisitions. *Magma NYN*. 2014;27:567-577.
23. Carr HY, Purcell EM. Effects of diffusion on free precession in nuclear magnetic resonance experiments. *Phys Rev*. 1954;94:630-638.
24. Allerhand A. Analysis of Carr–Purcell spin-echo NMR experiments on multiple-spin systems. I: The effect of homonuclear coupling. *J Chem Phys*. 1966;44:1-9.
25. Kim D, Jensen JH, Wu EX, Sheth SS, Brittenham GM. Breathhold multiecho fast spin-echo pulse sequence for accurate R2 measurement in the heart and liver. *Magn Reson Med*. 2009;62:300-306.
26. Hennig J. Multiecho imaging sequences with low refocusing flip angles. *J Magn Reson 1969*. 1988;78:397-407.
27. Zur Y. An algorithm to calculate the NMR signal of a multi spin-echo sequence with relaxation and spin-diffusion. *J Magn Reson*. 2004;171:97-106.
28. Lukzen NN, Petrova MV, Koptyug IV, Savelov AA, Sagdeev RZ. The generating functions formalism for the analysis of spin response to the periodic trains of RF pulses. Echo sequences with arbitrary refocusing angles and resonance offsets. *J Magn Reson*. 2009;196:164-169.
29. Prasloski T, Mädler B, Xiang Q-S, MacKay A, Jones C. Applications of stimulated echo correction to multicomponent T2 analysis. *Magn Reson Med*. 2012;67:1803-1814.
30. Huang C, Bilgin A, Barr T, Altbach MI. T2 relaxometry with indirect echo compensation from highly undersampled data. *Magn Reson Med*. 2013;70:1026-1037.
31. Petrovic A, Scheurer E, Stollberger R. Closed-form solution for T2 mapping with nonideal refocusing of slice selective CPMG sequences. *Magn Reson Med*. 2015;73:818-827.
32. Huang C, Altbach MI, El Fakhri G. Pattern recognition for rapid T2 mapping with stimulated echo compensation. *Magn Reson Imaging*. 2014;32:969-974.
33. McPhee KC, Wilman AH. Transverse relaxation and flip angle mapping: Evaluation of simultaneous and independent methods using multiple spin echoes. *Magn Reson Med*. 2017;77:2057-2065.
34. Weigel M. Extended phase graphs: Dephasing, RF pulses, and echoes—Pure and simple. *J Magn Reson Imaging JMRI*. 2015;41:266-295.
35. Cadzow JA. Signal enhancement—A composite property mapping algorithm. *IEEE Trans Acoust Speech Signal Process*. 1988;36:49-62.
36. Lebel RM. StimFit: A toolbox for robust T2 mapping with stimulated echo compensation. In: Proceedings from the 20th Annual Meeting of ISMRM, Melbourne, Australia, 2012. p 2588.
37. Pauly J, Le Roux P, Nishimura D, Macovski A. Parameter relations for the Shinnar-Le Roux selective excitation pulse design algorithm [NMR imaging]. *IEEE Trans Med Imaging*. 1991;10:53-65.
38. Martin BJ, Altman DG. Statistical methods for assessing agreement between two methods of clinical measurement. *Lancet*. 1986;327:307-310.
39. Koo TK, Li MY. A guideline of selecting and reporting intraclass correlation coefficients for reliability research. *J Chiropr Med*. 2016;15:155-163.
40. McPhee KC, Wilman AH. Limitations of skipping echoes for exponential T2 fitting. *J Magn Reson Imaging*. 2018;48:1432-1440.
41. Uddin M, Marc Lebel R,Wilman AH, et al. Transverse relaxometry with reduced echo train lengths via stimulated echo compensation. *Magn Reson Med*. 2013;70:1340-1346.
42. Kumar D, Hariharan H, Faizy TD, et al. Using 3D spatial correlations to improve the noise robustness of multi component analysis of 3D multi echo quantitative T2 relaxometry data. *NeuroImage*. 2018;178:583-601.

43. Radunsky D, Blumenfeld-Katzir T, Volovyk O, et al. Analysis of magnetization transfer (MT) influence on quantitative mapping of T2 relaxation time. *Magn Reson Med*. 2019;82:145-158.
44. Harrison R, Bronskill MJ, Henkelman RM. Magnetization transfer and T2 relaxation components in tissue. *Magn Reson Med*. 1995;33:490-496.
45. Oakden W, Stanisz GJ. Effects of diffusion on high-resolution quantitative T2 MRI. *NMR Biomed*. 2014;27:672-680.
46. Weigel M, Schwenk S, Kiselev VG, Scheffler K, Hennig J. Extended phase graphs with anisotropic diffusion. *J Magn Reson San Diego Calif 1997*, 2010;205:276-285.
47. Hargreaves BA, Miller KL. Using extended phase graphs: Review and examples. In: Proceedings of the 21st Annual Meeting of ISMRM, Salt Lake City, Utah, 2013. p 3718.
48. Scheffler K. A pictorial description of steady-states in rapid magnetic resonance imaging. *Concepts Magn Reson*. 1999;11:291-304.
49. Hennig J, Weigel M, Scheffler K. Calculation of flip angles for echo trains with predefined amplitudes with the extended phase graph (EPG)-algorithm: Principles and applications to hyperecho and TRAPS sequences. *Magn Reson Med*. 2004;51:68-80.
50. Ganter C. Analytical solution to the transient phase of steady-state free precession sequences. *Magn Reson Med*. 2009;62:149-164.
51. Weigel M, Zaitsev M, Hennig J. Inversion recovery prepared turbo spin echo sequences with reduced SAR using smooth transitions between pseudo steady states. *Magn Reson Med*. 2007;57:631-637.
52. Busse RF, Hariharan H, Vu A, Brittain JH. Fast spin echo sequences with very long echo trains: design of variable refocusing flip angle schedules and generation of clinical T2 contrast. *Magn Reson Med*. 2006;55:1030-1037.

SUPPORTING INFORMATION

Additional Supporting Information may be found online in the Supporting Information section.

FIGURE S1 The 24 randomly selected regions of interest in all 4 human subjects

FIGURE S2 The 10 selected regions of interest for quantitative analysis of T_2 values in a healthy volunteer as reported in Table 2

How to cite this article: Fatemi Y, Danyali H, Helfroush MS, Amiri H. Fast T_2 mapping using multi-echo spin-echo MRI: A linear order approach. *Magn Reson Med*. 2020;84:2815–2830. https://doi.org/10.1002/mrm.28309

APPENDIX

In this paper, the basic magnetization response of a MESE (CPMG-based) sequence with α_{ex} excitation flip angle, α_{ref} refocusing flip angles, and echo spacing *esp* has been investigated. According to Weigel,[34] the configuration states of a MESE-MRI sequence can be described by the different physical operators acting by means of successive operator matrix on the state matrix, $\boldsymbol{\Omega}(t)$, and modifying it to account for RF pulse transmit, relaxation, and dephasing effects[46,47] as follows:

$$\boldsymbol{\Omega}(t) = \ldots \boldsymbol{S}(\Delta k)\boldsymbol{E}\left(T_1, T_2, \tau\right)\boldsymbol{T}(\alpha, \phi)\boldsymbol{S}(\Delta k)\boldsymbol{E}\left(T_1, T_2, \tau\right)\boldsymbol{\Omega}(t=0). \tag{A1}$$

The operators $\boldsymbol{T}(\alpha, \phi)$, $\boldsymbol{E}\left(T_1, T_2, \tau\right)$, and $\boldsymbol{S}(\Delta k)$ representing RF pulse action, relaxation, and dephasing effects, respectively, will be introduced as follows.

$\boldsymbol{T}(\alpha, \phi)$ – Operator:

$\boldsymbol{T}(\alpha, \phi)$ operator propagates the configuration states through an RF rotation of α, with phase ϕ as follows:

$$\begin{bmatrix} \tilde{F}_k \\ \tilde{F}^*_{-k} \\ \tilde{Z}_k \end{bmatrix}^+ = \boldsymbol{T}(\alpha, \phi). \begin{bmatrix} \tilde{F}_k \\ \tilde{F}^*_{-k} \\ \tilde{Z}_k \end{bmatrix}^- \tag{A2}$$

where $\tilde{F}_k$, $\tilde{F}^*_{-k}$, and $\tilde{Z}_k$ denote configuration states of dephasing transverse magnetization, rephasing transverse magnetization, and modulated longitudinal magnetization, respectively. The k parameter describes dephasing of the state in units of 2π. The "+" and "−" symbols represent the magnetization right "before" and "after" application of the RF pulse, respectively. The operator $\boldsymbol{T}(\alpha, \phi)$ is defined as the following 3 × 3 matrix:

$$\boldsymbol{T}(\alpha, \phi) = \begin{bmatrix} \cos^2\frac{\alpha}{2} & e^{2i\phi}\sin^2\frac{\alpha}{2} & -ie^{i\phi}\sin\alpha \\ e^{-2i\phi}\sin^2\frac{\alpha}{2} & \cos^2\frac{\alpha}{2} & ie^{-i\phi}\sin\alpha \\ -\frac{i}{2}e^{-i\phi}\sin\alpha & \frac{i}{2}e^{i\phi}\sin\alpha & \cos\alpha \end{bmatrix}$$

$\boldsymbol{E}\left(T_1, T_2, \tau\right)$ – Operator:

As denoted by Weigel,[34] the operator $\boldsymbol{E}\left(T_1, T_2, \tau\right)$, with the spin-lattice relaxation time T_1, the spin-spin relaxation time T_2, and the time interval τ can be used for the representation of relaxation effects as follows:

For $k = 0$:

$$\begin{bmatrix} F \\ F^* \\ Z \end{bmatrix}^+ = \boldsymbol{E}\left(T_1, T_2, \tau\right). \begin{bmatrix} F \\ F^* \\ Z \end{bmatrix}^- + \begin{bmatrix} 0 \\ 0 \\ 1 - e^{-\frac{\tau}{T_1}} \end{bmatrix}$$

And for $k \neq 0$:

$$\begin{bmatrix} \tilde{F}_k \\ \tilde{F}^*_{-k} \\ \tilde{Z}_k \end{bmatrix}^+ = \boldsymbol{E}\left(T_1, T_2, \tau\right). \begin{bmatrix} \tilde{F}_k \\ \tilde{F}^*_{-k} \\ \tilde{Z}_k \end{bmatrix}^-$$

where

$$\boldsymbol{E}\left(T_1,T_2,\tau\right)=\begin{bmatrix} e^{-\frac{\tau}{T_2}} & 0 & 0 \\ 0 & e^{-\frac{\tau}{T_2}} & 0 \\ 0 & 0 & e^{-\frac{\tau}{T_1}} \end{bmatrix} \quad \text{(A3)}$$

$\boldsymbol{S}(\Delta k)$ – Operator:

The shift operator $\boldsymbol{S}(\Delta k)$ has been used to account for dephasing effects on the configuration states caused by gradients[48-52]:

$$\boldsymbol{S}(\Delta k):\ \tilde{F}_k \rightarrow \tilde{F}_{k+\Delta k} \quad \text{and } \tilde{Z}_k \rightarrow \tilde{Z}_k \quad \text{(A4)}$$

The MESE Sequence Formulation

The configuration states of a MESE sequence can be simulated based on the EPG framework using Equation (A1). Initially, the $\boldsymbol{T}(\alpha,\phi)$ operators of the RF pulses should be defined. In accordance with the CPMG condition, the phase of the excitation RF pulse, α_{ex}, is $\phi=90°$ (y-axis), whereas the phase of all refocusing RF pulses, α_{ref}, is $\phi=0°$ (x-axis):

$$\boldsymbol{T}\left(\alpha_{ex},90°\right)=\begin{bmatrix} \cos^2\frac{\alpha_{ex}}{2} & -\sin^2\frac{\alpha_{ex}}{2} & \sin\alpha_{ex} \\ -\sin^2\frac{\alpha_{ex}}{2} & \cos^2\frac{\alpha_{ex}}{2} & \sin\alpha_{ex} \\ -\frac{1}{2}\sin\alpha_{ex} & -\frac{1}{2}\sin\alpha_{ex} & \cos\alpha_{ex} \end{bmatrix}$$

and

$$\boldsymbol{T}\left(\alpha_{ref},0°\right)=\begin{bmatrix} \cos^2\frac{\alpha_{ref}}{2} & \sin^2\frac{\alpha_{ref}}{2} & -i\sin\alpha_{ref} \\ \sin^2\frac{\alpha_{ref}}{2} & \cos^2\frac{\alpha_{ref}}{2} & i\sin\alpha_{ref} \\ -\frac{i}{2}\sin\alpha_{ref} & \frac{i}{2}\sin\alpha_{ref} & \cos\alpha_{ref} \end{bmatrix}.$$

At the beginning, the initial state matrix is $\Omega(t<0)=\begin{bmatrix} 0 & 0 & M_0 \end{bmatrix}^T$, where M_0 is the longitudinal magnetization before excitation at the equilibrium magnetization state. The excitation pulse is applied at $t=0$, which changes the state matrix as follows:

$$\boldsymbol{\Omega}(t=0)=\boldsymbol{T}\left(\alpha_{ex},90°\right)\ \boldsymbol{\Omega}(T<0)=\begin{bmatrix} F_0 \\ F_0^* \\ Z_0 \end{bmatrix}=\begin{bmatrix} M_0\sin\alpha_{ex} \\ M_0\sin\alpha_{ex} \\ M_0\cos\alpha_{ex} \end{bmatrix}. \quad \text{(A5)}$$

Now, we have the state matrix at $t=0$. Next, relaxation and recovery effects are performed by applying the $\boldsymbol{E}\left(T_1,T_2,\tau\right)$ operator. After that, the shift operator $\boldsymbol{S}(\Delta k)$ changes the states using the transition rule of the time evolution (it should be noted that the shift operator expands the columns of the state matrix by means of expansion rules defined in Equation (A4)) as follows:

$$\boldsymbol{\Omega}\left(t=\frac{1}{2}esp^-\right)=\boldsymbol{S}(\Delta k)\ \boldsymbol{E}\left(T_1,T_2,\tau\right)\ \boldsymbol{\Omega}(t=0)=\begin{bmatrix} 0 & E_2M_0\sin\alpha_{ex} \\ 0 & 0 \\ E_1M_0\cos\alpha_{ex} & 0 \end{bmatrix}, \quad \text{(A6)}$$

where $\Delta k=1$ and (for simplicity) $E_1=\exp\left(-\tau/T_1\right)$ and $E_2=\exp\left(-\tau/T_1\right)$. At $t=\frac{1}{2}esp$, the first refocusing pulse is applied by predefined $\boldsymbol{T}\left(\alpha_{ref},0°\right)$ operator (ie, refocusing RF pulse action with CPMG condition) as follows:

$$\boldsymbol{\Omega}\left(t=\frac{1}{2}esp^+\right)=\boldsymbol{T}\left(\alpha_{ref},0°\right)\ \boldsymbol{\Omega}\left(t=\frac{1}{2}esp^-\right)=\begin{bmatrix} -i\sin\alpha_{ref}\left(E_1M_0\cos\alpha_{ex}-E_1+1\right) & E_2M_0\cos^2\frac{\alpha_{ref}}{2}\sin\alpha_{ex} \\ i\sin\alpha_{ref}\left(E_1M_0\cos\alpha_{ex}-E_1+1\right) & E_2M_0\sin^2\frac{\alpha_{ref}}{2}\sin\alpha_{ex} \\ \cos\alpha_{ref}\left(E_1M_0\cos\alpha_{ex}-E_1+1\right) & -\frac{i}{2}E_2M_0\sin\alpha_{ref}\sin\alpha_{ex} \end{bmatrix} \quad \text{(A7)}$$

Subsequently, to complete the first echo experience at $t=esp$, the same $\boldsymbol{E}\left(T_1,T_2,\tau\right)$ and $\boldsymbol{S}(\Delta k)$ operators in which $\Delta k=1$ are applied:

$$\boldsymbol{\Omega}(t=esp)=\boldsymbol{S}(\Delta k)\ \boldsymbol{E}\left(T_1,T_2,\tau\right)\ \boldsymbol{\Omega}\left(t=\frac{1}{2}esp^+\right)=\begin{bmatrix} \sin\alpha_{ex}M_0E_2^2\sin^2\frac{\alpha_{ref}}{2} & -iE_2\sin\alpha_{ref}\left(E_1M_0\cos\alpha_{ex}-E_1+1\right) & \sin\alpha_{ex}M_0E_2^2\cos^2\frac{\alpha_{ref}}{2} \\ \sin\alpha_{ex}M_0E_2^2\sin^2\frac{\alpha_{ref}}{2} & 0 & 0 \\ E_1\cos\alpha_{ref}\left(E_1M_0\cos\alpha_{ex}-E_1+1\right)-E_1+1 & -\frac{i}{2}E_1E_2M_0\sin\alpha_{ex}\sin\alpha_{ref} & 0 \end{bmatrix}$$

Only $\tilde{F}(0)$-states (ie, $\boldsymbol{\Omega}_{1,1}$) contribute to echo formation and the signal intensity at each echo, because the other states ($\tilde{F}_+$ and $\tilde{F}_-$) are fully dephased. Therefore, the equation of the first echo can be written as

$$Y_1=M_0\sin\alpha_{ex}E_2^2\sin^2\frac{\alpha_{ref}}{2}. \quad \text{(A8)}$$

By repeating the same operators, just like the first echo operators from $t\geq 1$, the equations of the other echoes can be calculated as

$$\boldsymbol{\Omega}(t=m\,esp)=\boldsymbol{S}(\Delta k)\boldsymbol{E}\left(T_1,T_2,\tau\right)\boldsymbol{T}\left(\alpha_{ref},0°\right)\boldsymbol{S}(\Delta k)\boldsymbol{E}\left(T_1,T_2,\tau\right)\boldsymbol{\Omega}(t=(m-1)\,esp). \quad \text{(A9)}$$

According to Equation (A9), the second and third echoes are

$$Y_2=M_0\sin\alpha_{ex}\left(E_2^4\sin^4\frac{\alpha_{ref}}{2}+\frac{1}{2}E_2^2E_1^2\sin^2\alpha_{ref}\right)$$

$$Y_3 = M_0 \sin\alpha_{ex} \left(E_2^6 \left(\sin^6\frac{\alpha_{ref}}{2} + \cos^4\frac{\alpha_{ref}}{2}\sin^2\frac{\alpha_{ref}}{2}\right) + E_2^4 E_1^2 \sin^2\frac{\alpha_{ref}}{2}\sin^2\alpha_{ref} + \frac{1}{2}E_2^2 E_1^4 \cos\alpha_{ref}\sin^2\alpha_{ref}\right).$$

The $\boldsymbol{Y} = \begin{bmatrix} Y_1 & Y_2 & Y_3 \end{bmatrix}^T$ equations can be displayed in a matrix form as follows:

$$\boldsymbol{Y} = M_0 \sin\alpha_{ex} \left(\left[\boldsymbol{G}\left(E_1\right) \circ \boldsymbol{\Gamma}\left(\alpha_{ref}\right)\right] \cdot \boldsymbol{S}\left(E_2\right)\right), \quad \text{(A10)}$$

where

$$\boldsymbol{G}\left(E_1\right) = \begin{bmatrix} 1 & 0 & 0 \\ E_1^2 & 1 & 0 \\ E_1^4 & E_1^2 & 1 \end{bmatrix}$$

$$\boldsymbol{\Gamma}\left(\alpha_{ref}\right) = \begin{bmatrix} \sin^2\frac{\alpha_{ref}}{2} & 0 & 0 \\ \frac{1}{2}\sin^2\alpha_{ref} & \sin^4\frac{\alpha_{ref}}{2} & 0 \\ \frac{1}{2}\cos\alpha_{ref}\sin^2\alpha_{ref} & \sin^2\frac{\alpha_{ref}}{2}\sin^2\alpha_{ref} & \sin^6\frac{\alpha_{ref}}{2} + 1\cos^4\frac{\alpha_{ref}}{2}\sin^2\frac{\alpha_{ref}}{2} \end{bmatrix},$$

$$\boldsymbol{S}\left(E_2\right) = \begin{bmatrix} E_2^2 \\ E_2^4 \\ E_2^6 \end{bmatrix}.$$

The $\boldsymbol{G}\left(E_1\right)$ is a unit lower triangular matrix with $ETL \times ETL$ size; $\boldsymbol{\Gamma}\left(\alpha_{\text{ref}}\right)$ is a lower triangular matrix with $ETL \times ETL$ size; and the $\boldsymbol{S}\left(E_2\right)$ is a vector with ETL elements. The symbol "$\circ$" denotes the Hadamard product. Based on Equation (A10), the general equation for the mth echo, Y_m, based on the EPG framework will be

$$Y_m = M_0 \sin\alpha_{ex} \sum_{i=1}^{m} \boldsymbol{G}_{m,i}\left(E_1\right) \boldsymbol{\Gamma}_{m,i}\left(\alpha_{ref}\right) \boldsymbol{S}_i\left(E_2\right), \quad \text{(A11)}$$

where

$$E_1 = e^{-\frac{esp}{2T_1}},\ E_2 = e^{-\frac{esp}{2T_2}}.$$

In this paper, we have extended Equation (A11) based on the SEPG model to account for the variation of the RF flip angles. Based on the SEPG model, the signal intensity $\boldsymbol{Y}$ is an aggregate of echo amplitudes integrated over the slice direction (z) as follows:

$$\boldsymbol{Y} = \sum_{z=1}^{Z} M_0 \sin\alpha_{ex}(z) \left(\left[\boldsymbol{G}\left(E_1\right) \circ \boldsymbol{\Gamma}\left(\alpha_{ref}(z)\right)\right] \cdot \boldsymbol{S}\left(E_2\right)\right). \quad \text{(A12)}$$

Note that Equation (A12) is presented in the matrix form. Finally, the general equation for mth echo, Y_m, based on the SEPG model can be written as

$$Y_m = \sum_{i=1}^{m} M_0 \boldsymbol{S}_i\left(E_2\right) \boldsymbol{G}_{m,i}\left(E_1\right) \left[\sum_{z=1}^{Z} \sin\left(\alpha_{ex}(z)\right) \boldsymbol{\Gamma}_{m,i}\left(\alpha_{ref}(z)\right)\right]. \quad \text{(A13)}$$